SURFACE AND CLEAR-SKY ALBEDOS AND EMISSIVITIES FROM MODIS AND VIRS WITH APPLICATION TO SEVIRI

P. Minnis and D. F. Young

NASA Langley Research Center
Mail Stop 420, Hampton, Virginia USA 23681-2199

D. R. Doelling

AS&M, Inc.
1 Executive Pkwy., Hampton, Virginia USA 23666

Sunny Sun-Mack, Yan Chen, Qing Z. Trepte

SAIC
1 Executive Pkwy., Hampton, Virginia USA 23666

Extended Abstract
Proceedings of the 2002 EUMETSAT Meteorological Satellite Conference
Dublin, Ireland
September 2 - 6, 2002

SURFACE AND CLEAR-SKY ALBEDOS AND EMISSIVITIES FROM MODIS AND VIRS WITH APPLICATION TO SEVIRI

P. Minnis and D. F. Young

NASA Langley Research Center
Mail Stop 420, Hampton, Virginia USA 23681-2199

D. R. Doelling

AS&M, Inc.
1 Executive Pkwy., Hampton, Virginia USA 23666

Sunny Sun-Mack, Yan Chen, Qing Z. Trepte

SAIC
1 Executive Pkwy., Hampton, Virginia USA 23666

ABSTRACT

Accurate knowledge of the geographical, temporal, and angular variabilities of albedo and emissivity is needed to reliably retrieve surface and cloud properties from satellite data. The upcoming spinning Enhanced Visible and Infrared Imager (SEVIRI) on the Meteosat Second Generation (MSG) satellite will provide unprecedented temporal coverage of Europe, Africa, and western Asia at several wavelengths including the narrowband visible (0.64 μm), near-infrared (1.64 μm), solar-infrared (3.92 μm), and infrared window (8.7 μm) channels. Several of the SEVIRI channels are close to channels on the Terra Moderate Resolution Imaging Spectroradiometer (MODIS) and the Tropical Rainfall Measuring Mission (TRMM) Visible Infrared Scanner (VIRS). A variety of algorithms developed by the Clouds and Earth's Radiant Energy System Project have been applied to the MODIS and VIRS data to derive surface emissivities at 3.7, 8.55, 10.8, and 12.0 μm over the globe at a 10' resolution for different surface types during all seasons. Similarly, clear-sky and surface albedos have been derived from the same datasets at 0.64 and 1.64 μm. The means and standard deviations were computed for each IGBP surface type for each season. Emissivities for the 3.7 and 8.5-μm channels were smaller than those for the other thermal channels. The emissivities and albedos were smallest and largest, respectively, over the Sahara Desert. The greatest errors in the retrievals of the albedos and emissivities are due to uncertainties in the bidirectional reflectance patterns at 1.64 and 3.7 μm, the viewing angle dependence of the surface emissivities, and the atmospheric moisture profiles used to

remove atmospheric effects. Multi-satellite views by MODIS, SEVIRI, and VIRS may be useful for minimizing some of the errors. The results should be valuable for immediate application to remote sensing by SEVIRI with updates as SEVIRI data become available.

1. INTRODUCTION

Surface albedo and emissivity vary with wavelength, soil type and moisture content, and vegetation type and condition as well as viewing and solar zenith angles. Because of these dependencies, the spectral variations of these two key parameters are valuable for remote sensing of surface properties and for detection of clouds and aerosols and retrievals of their properties. Accurate knowledge of the geographical, temporal, and angular variabilities of albedo and emissivity is needed to reliably retrieve surface and cloud properties from satellite data. The upcoming SEVIRI on the MSG satellite will provide unprecedented temporal coverage of Europe, Africa, and western Asia at several wavelengths. To begin cloud detection and retrieval from SEVIRI, it is necessary to establish initial values of emissivity and clear-sky reflectance for the SEVIRI spectral channels that include some wavelengths heretofore unavailable on geostationary satellites. This paper describes the development of a clear-sky database that can serve as a startup for analyzing clouds from SEVIRI data.

The database relies on analyses performed on data from the Terra MODIS and the TRMM VIRS that were taken over areas determined to be clear by the cloud algorithm (e.g., Minnis et al. 2002a) developed for the Clouds and Earth's Radiant Energy System (CERES; *Wielicki et al.* 1998). The data are used in conjunction with models designed to account for atmospheric absorption and anisotropic reflectance to predict the clear-sky reflectances at a 10' resolution and the clear-sky brightness temperatures at 4 wavelengths at a gridded resolution of 1° x 1°. Initial analyses of SEVIRI data in conjunction with this database should allow for rapid updating of the SEVIRI clear-sky spectral database.

2. DATA AND MODELS

The 1-km MODIS data are sampled at every other pixel and scan line by CERES to obtain an effective 2-km resolution. MODIS channels 1, 2, 6, 20, 29, 31, and 32 with central wavelengths at 0.645, 0.858, 1.64, 3.75, 8.55, 11.03, and 12.02 μm have counterparts on SEVIRI at similar but slightly different wavelengths, except for 8.55 μm, which corresponds to SEVIRI's 8.7 μm. These MODIS channels are used to determine overhead-sun albedos $\alpha_{o\lambda}$ at solar wavelengths and surface emissivities ε_λ at thermal wavelengths for use with SEVIRI data analyses. Only MODIS data taken during April 2001 are used in this study. For simplicity, the wavelength subscript is dropped in the following discussion except where appropriate.

The solar zenith angle (SZA) dependence of clear-sky albedo for a given surface can be described with a normalized directional reflectance model

$$\delta(\mu_o) = \alpha(\mu_o) / \alpha_o, \qquad (1)$$

where μ_o is the cos(SZA) and the albedo is

$$\alpha(\mu_o) = \rho(\mu_o,\mu,\phi) / \chi(K; \mu_o,\mu,\phi). \qquad (2)$$

In (2), K is the IGBP surface type, χ is the bidirectional reflectance distribution function (BRDF), μ is the cosine of the viewing zenith angle, ϕ is the relative azimuth angle, and the measured top-of

atmosphere (TOA) reflectance is ρ. For the 0.645 and 0.858-μm data, the raw TOA reflectances are used. However, for the 1.64-μm data, a simple atmospheric correction is applied, ignoring aerosol effects, to estimate the surface reflectance (Sun-Mack et al. 1999). Therefore, in this study, ρ corresponds to clear-sky TOA reflectance for channels 1 and 2, but to surface reflectance for channel 6.

The BRDFs from Minnis and Harrison (1984) and Suttles et al. (1988) are used for ocean and all other surfaces, respectively, for channels 1 and 2. At 1.64 μm, a theoretical BRDF is used for snow while the ocean, desert, and vegetated land BRDFs are taken from Minnis and Harrison (1984), Suttles et al. (1988), and Kriebel (1978), respectively. The Kriebel (1978) models, corresponding to four different vegetation types, are applied to the most similar IGBP surface types. Values for the normalized directional reflectance models are taken from Sun-Mack et al. (1999) and Chen et al. (2002).

A simple radiative transfer model using the correlated *k*-distribution method (Kratz 1995) with coefficients for the MODIS wavelengths (e.g., Minnis et al. 2002b) is used to account for atmospheric absorption at thermal wavelengths using profiles of atmospheric temperature, humidity, and ozone. The profiles are taken from European Center for Medium Range Forecast (ECMWF) analyses generated for CERES.

3. OVERHEAD SUN ALBEDO ESTIMATION

For a given location, a measurement of $\rho(\mu_o,\mu,\phi)$ is converted to α_o using (1) and (2). Because a location cannot be precisely matched with a single pixel during each overpass, a mean value of reflectance and its standard deviation (SD) are computed for a given region for an overpass. To initialize the albedos, clear-sky 0.65-μm reflectances from the International Satellite Cloud Climatology (ISCCP) Advanced Very High Resolution Radiometer (AVHRR) DX were converted to α_o and averaged for 1 month in each season during 1986 on a 1° grid. Temporal and spatial SDs were computed for each region. Mean values were computed for each IGBP surface type and used to assign albedos and SDs to boxes with no clear AVHRR data. These albedos were then used in the cloud mask of Trepte et al. (1999) to determine clear pixels in VIRS data for the CERES cloud algorithm. Mean reflectances were computed from the VIRS 0.65 and 1.6-μm data and used to compute α_o for a 10' regional grid. The original DX value of α_o was replaced with an average of the two values if the new value differed by more then one SD from the original value. In this manner, the spatial resolution and accuracy of the clear-sky albedo field was increased. New IGBP means and SD were also computed and used to fill in missing albedos. The process was repeated again with Terra MODIS data using the VIRS updated albedos for the month of April. Only results for the 0.64 and 1.64-μm channels are presented.

4. SURFACE EMISSIVITY RETRIEVALS

Surface emissivity is estimated by solving a set of simultaneous equations to first obtain the skin temperature T_{skin}. The method requires observations from both daytime and nighttime over the same area. The relationship between the TOA and surface radiances can be represented as

$$B_i(T_i) = \varepsilon_{ai}B_i(T_{ai}) + (1- \varepsilon_{ai})B_i(T_{si}) \qquad (3)$$

where B is the Planck function, ε_a and T_a are the atmospheric effective emissivity and effective temperature, respectively. The radiance for T_{si}, the effective skin radiating temperature for channel i,

is determined by adjusting the radiance for atmospheric absorption and emission. In the absence of solar radiation, the radiation balance at surface is

$$B_i(T_{si}) = \varepsilon_i B_i(T_{skin}) + (1- \varepsilon_i) L_{ai} \quad (4)$$

where the downwelling atmospheric radiance at the surface is L_a. It assumed that ε_i does not depend on μ. At night,

$$T_{skin} = B_i^{-1}[\{B_i(T_{si}) - L_{ai}\}/ \varepsilon_i + L_{ai}], \quad (5)$$

where B_i^{-1} is the inverse Planck function. If the skin temperature is known, the emissivity can be solved for the remaining channels, e.g., for channel 20,

$$\varepsilon_{20} = [B_{20}(T_{s20}) - L_{a20} / [B_{20}(T_{skin}) - L_{a20}]. \quad (6)$$

At night, both T_{s20} and T_{s31} can be derived using (4) and the emissivity ratio,

$$\varepsilon_{20}' = \varepsilon_{20} /\varepsilon_{31} = [B_{20}(T_{s20}) - L_{a20}] / [B_{20}(T_{s31}) - L_{a20}], \quad (7)$$

can be computed. If it is assumed that the ratio is a constant for a given location during both day and night, then the value of ε_{20} can be determined from daytime data. However, the ratio varies with L_{a3}, which changes with the column precipitable water PW. To account for this variation, the data are fitted to

$$\varepsilon_{20}' = \varepsilon_{20o}' + a\, PW + b\, PW^2, \quad (8)$$

where ε_{20o}' is the baseline emissivity ratio and is generally close to the value obtained from (7) if L_{a20} = 0. The coefficients for (8) are computed from data taken during the night for several different times to obtain a reasonable dynamic range in PW. During the daytime, the apparent channel-20 surface temperature is

$$B_{20}(T_{s20}) = \varepsilon_{20} [B_{20}(T_{skin})] + \alpha_{20} [\chi S_{20}' + L_{a20}], \quad (9)$$

where the value of χ is taken form the models used for the 0.65 reflectance, α_{20} is the surface albedo, and S_{20}', the solar radiation reaching the surface, is computed from the Earth-sun distance and μ_o-corrected solar constant attenuated by atmospheric absorption. According to the Kirchoff's law,

$$\varepsilon_{20} = (1- \alpha_{20}). \quad (10)$$

Using (6), (7), and (10) to substitute for the emitted component and the albedo on the right hand side of (9) and rearranging gives

$$\varepsilon_{20} = 1 - \{B_{20}(T_{s20}) - \varepsilon_{20}' [B_{20}(T_{s31})] - (1 - \varepsilon_{20}') L_{a20}\} / \chi S_{20}'. \quad (11)$$

In this manner, ε_{20} is derived using (11). The absorption coefficients used for the thermal component are applied to the observed 3.7-μm radiance to obtain $B_{20}(T_{s20})$. Although the atmospheric attenuation of the upwelling solar and emitted 3.7-μm radiances is slightly different for each component, the differences should have a negligible impact on the result. Knowing ε_{20}, T_{skin} can easily be solved from (11). Then, ε_{31}, ε_{32}, and ε_{29} are computed from (5).

This technique was tested theoretically using 3 different surface types with ε_{20} ranging from 0.73 to 0.97 and ε_{31} ranging 0.93 to 0.99 using 91 soundings to represent a large range of atmospheric conditions. Previously, ISCCP DX AVHRR data taken during 1986 were processed using the same method as mentioned above to obtain channel 20, 31, and 32 emissivity maps. The resulting values of ε_{20} from ISCCP DX data were within 1% of the original value for all of the cases with the largest errors occurring for the desert (0.73) case. RMS errors up to 3% were found for ε_{31} with the greatest errors occurring for the desert case. The mean errors were all negligible. The theoretical calculations assumed an isotropic surface reflectance and no μ_o-dependence of ε.

The MODIS data were analyzed by computing ε_{20}' for each clear nighttime pixel and averaging the results for every 1° latitude-longitude box for a given orbit. The corresponding value of *PW* was saved for each 1° box. Because of insufficient sampling, a mean value of ε_{20}' was computed for each region and used instead of a fit to (8) to derive ε_i for all channels from the daytime data to obtain means and standard deviations for each region. Averages were also computed for each IGBP surface type (Table 1) and then used to fill in values for regions with no data.

Table 1. IGBP type and mean surface emissivity and standard deviation from MODIS, April 2001.

TYPE		3.9 μm		10.8 μm		12.0 μm		8.7 μm	
1 evergreen needle	107	0.962	0.012	0.988	0.004	0.984	0.007	0.963	0.041
2 evergreen broad	3614	0.941	0.010	0.978	----	0.972	0.020	0.953	0.026
4 dec. broad	80	0.940	0.018	0.979	0.010	0.976	0.022	0.951	0.035
5 mixed forest	25	0.948	0.012	0.983	0.005	0.980	0.010	0.961	0.045
6 closed shrub	912	0.911	0.043	0.969	0.019	0.961	0.040	0.914	0.073
7 open shrubs	2712	0.829	0.064	0.948	0.018	0.959	0.022	0.855	0.084
8 woody savanna	5457	0.935	0.013	0.976	0.010	0.970	0.023	0.936	0.047
9 savannas	6748	0.914	0.024	0.968	0.012	0.965	0.010	0.921	0.061
10 grasslands	2121	0.894	0.036	0.967	0.012	0.971	0.012	0.919	0.051
11 wetlands	30	0.951	0.029	0.973	0.025	0.941	0.070	0.970	0.027
12 croplands	18312	0.927	0.021	0.974	0.009	0.972	0.015	0.941	0.057
13 urban	20	0.931	0.030	0.973	0.008	0.961	0.007	0.917	0.115
14 mosaic	5988	0.934	0.017	0.975	0.007	0.969	0.019	0.933	0.066
16 desert	10869	0.758	0.053	0.934	0.010	0.963	0.013	0.757	0.080

5. RESULTS

Figure 1 shows the emissivities derived from MODIS for April 2001. All values over water surfaces should be ignored as they are not valid. The 3.7-μm values range from 0.6 to 0.98 while the 8.5-μm emissivities vary from 0.55 to 0.98. The values are considerably smaller for the longer wavelengths with minimum values near 0.90 at both 11 and 12 μm. The smallest values at all wavelengths occur over desert areas while the largest emissivities are found over forested regions.

The IGBP means and standard deviations are listed in Table 1. The greatest variations with scene type occur for the 8.5-μm channel suggesting that it may be more susceptible to moisture or vegetation changes than the other wavelengths. The mean daytime errors in 3.7-μm temperatures computed using the derived emissivities averaged less than 1 K with a standard deviation of ~4.5 K. At night, the mean errors reduced to less than 0.5 K with a SD of ~ 3 K. The uncertainties for the other channels were much less. Uncertainties are due to possible day-night changes in the emissivity with changing moisture content of the vegetation and soil, errors in the atmospheric soundings, aerosol effects, viewing-zenith angle dependencies, and the use of visible-channel BRDFs for 3.7-μm. The

use of the BRDFs was found to improve the results compared to those derived using a Lambertian reflectance assumption. Values were not computed for ocean, tundra, snow, or coastline. Snow emissivities are estimated using radiative transfer calculations assuming an ice cloud composed of hexagonal columns with an effective particle diameter of 135 μm and an optical depth of 1000 can be used to represent snow. The model of Masuda et al. (1988) was used for ocean surfaces.

The clear-sky overhead sun albedos are shown in Fig. 2 for April 2001. The 0.64-μm albedos range from 0.06 over water to more 0.5 over parts of the Sahara Desert. The desert albedos are highly variable depending on the rock types, moisture content, and vegetation coverage. The 1.6-μm albedos are more variable ranging from 0.03 over water to 0.80 over parts of the Sahara Desert. Again, the desert albedo variability is much greater than that seen for other surface types.

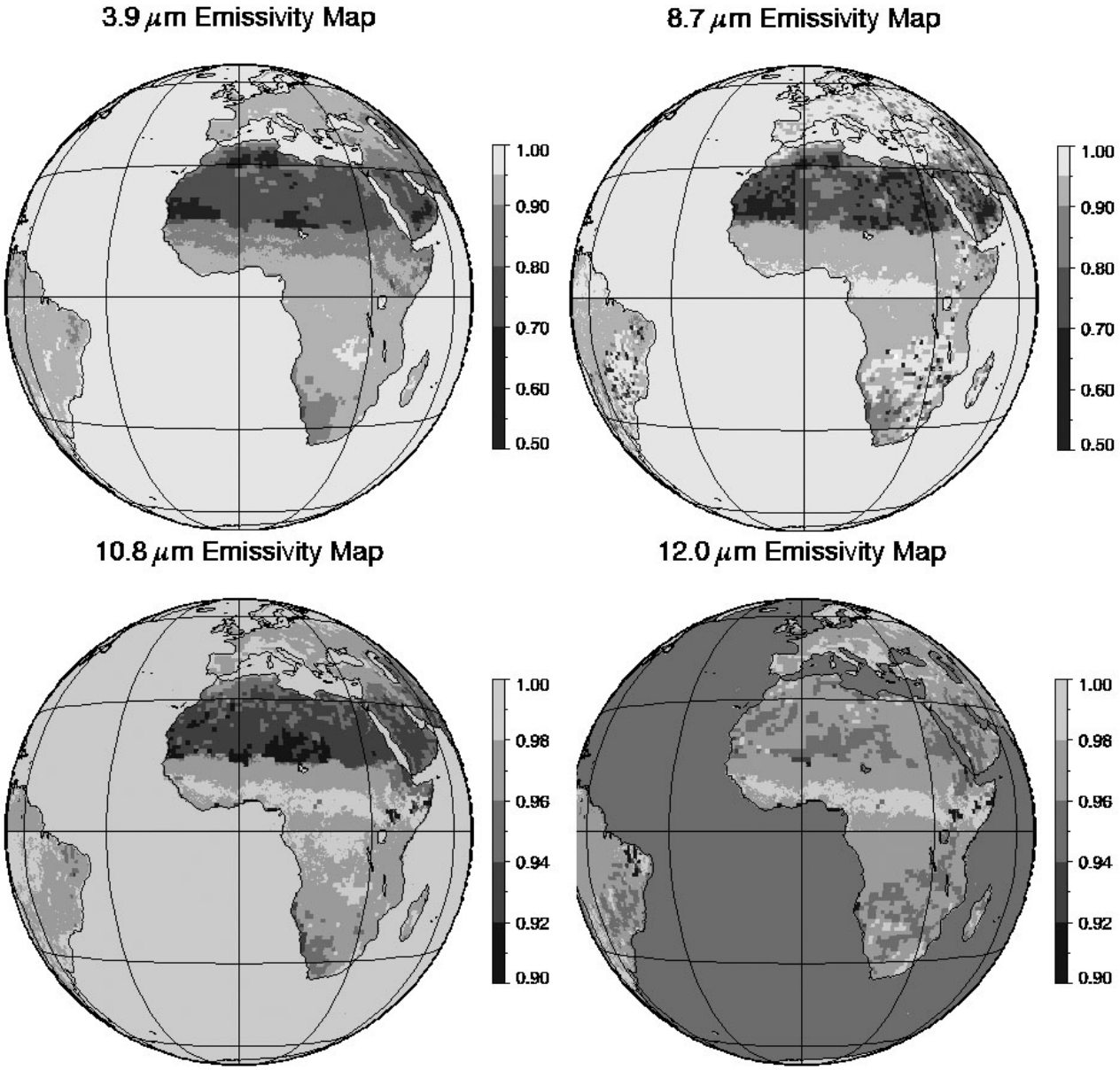

Fig. 1. Surface emissivities from MODIS, April 2001.

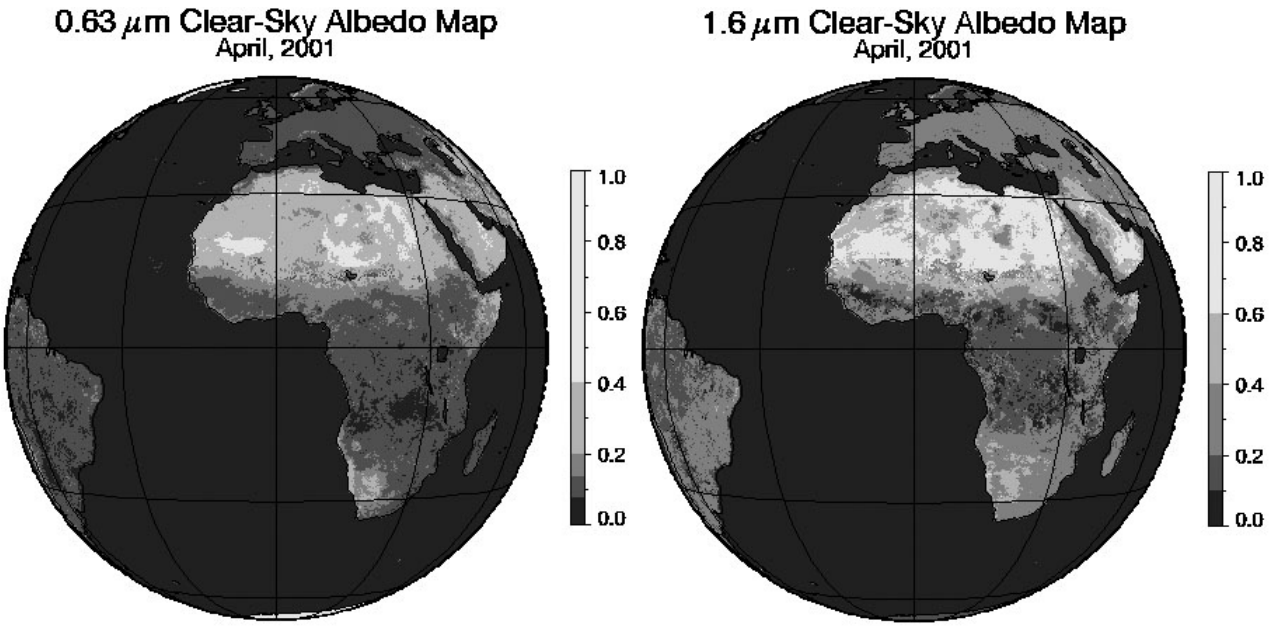

Fig. 2. Overhead-sun albedo derived from MODIS channels 1 and 6.

This variability is illustrated better in Table 2, which lists the mean albedos and standard deviations for each IGBP surface type. The 1.6-μm albedos and standard deviations are typically twice as large as their visible-channel counterparts. Evergreen needleleaf forests are the most homogeneous land type with the smallest standard deviations for each wavelength. The open shrublands and deserts have the largest standard deviations in both wavelengths. These derive albedos are subject to uncertainties that arise from the use of single directional reflectance models for each surface type. The SZA dependence may not vary much within the different forest types because of the small variability in the derived albedos. However, use of the same values of δ for all deserts could result in overestimation of α_o for brighter deserts and underestimates for darker deserts. Variability may also arise from episodic aerosol changes over a given surface and from the use of limited BRDF models. More scene specific BRDFs would probably improve the accuracy of the derived albedos.

Table 2. IGBP type and mean clear-sky albedo and standard deviation from MODIS, April 2001.

IGBP TYPE	0.63 μm		1.6 μm	
1 evergreen needleleaf	0.0893	0.0058	0.1729	0.0199
2 evergreen broadleaf	0.0991	0.0184	0.1728	0.0351
4 deciduous broadleaf	0.0961	0.0157	0.2086	0.0552
5 mixed forests	0.0978	0.0086	0.1886	0.0426
6 closed shrublands	0.1337	0.0356	0.1883	0.0682
7 open shrubland	0.2133	0.0714	0.4527	0.1602
8 woody savannas	0.1067	0.0246	0.1284	0.0477
9 savannas	0.1260	0.0433	0.3059	0.1048
10 grasslands	0.1670	0.0584	0.3743	0.1229
11 permanent wetlands	0.0874	0.0244	0.1943	0.0685
12 croplands	0.1109	0.0190	0.2546	0.0504
13 urban	0.0996	0.0357	0.1598	0.0906
14 mosaic	0.1023	0.0251	0.2440	0.0707
16 desert	0.3135	0.0821	0.5554	0.1511
17 water	0.0616	0.0033	0.0301	0.0040

6. CONCLUDING REMARKS

The initial results from MODIS provide surface albedo and emissivity values for new wavelengths that should enable improved retrieval of surface and cloud properties. Both of these channels have SEVERI counterparts on MSG. The SEVIRI data can be used to attack a wide variety of remote sensing problems that could not be addressed with earlier instruments because of poor spectral, spatial, or temporal sampling. The combination of the algorithms described above with the additional channels from SEVERI will greatly enhance the quality of cloud products from geostationary satellites. It should be possible to process full disc SEVIRI data every 30 minutes and derive updated results for each channel facilitating the study of albedo and emissivity at higher temporal and spatial resolutions.

REFERENCES

Chen, Y., S. Sun-Mack, Q. Z. Trepte, P. Minnis, and D. F. Young, 2002: Solar zenith angle variation of clear-sky narrowband albedos derived from VIRS and MODIS. *Proc. 11th AMS Conf. Atmos. Rad.*, Ogden, UT, June 3-7, 152-155.

Kratz, D. P., 1995: The correlated k-distribution technique as applied to the AVHRR channels. *J. Quant. Spectrosc. Radiat. Transfer*, **53**, 501-507.

Kriebel, K. T., 1978: Measured spectral bidirectional reflectance properties of vegetated surfaces. *Appl. Opt.*, **17**, 253-259.

Masuda, K., T. Takashima, and Y. Takayama, 1988: Emissivity of pure and sea waters for the model sea surface in the infrared window regions. *Remote Sens. Environ.*, **24**, 313-329.

Minnis, P. and E. F. Harrison, 1984: Diurnal variability of regional cloud and clear-sky radiative parameters derived from GOES data, Part I: Analysis method. *J. Clim.Appl. Meteorol.*, **23**, 993-1011.

Minnis, P., L. Nguyen, D. R. Doelling, D. F. Young, W. F. Miller, and D. P. Kratz, 2002b: Rapid calibration of operational and research meteorological satellite imagers, Part II: Comparison of infrared channels. In press, *J. Atmos. Oceanic Technol.*

Minnis, P., D. F. Young, B. A. Wielicki, D. P. Kratz, P. W. Heck, S. Sun-Mack, Q. Z. Trepte, Y. Chen, S. L. Gibson, R. R. Brown, 2002a: Seasonal and diurnal variations of cloud properties derived for CERES from VIRS and MODIS data. *Proc. 11th AMS Conf. Atmos. Rad.*, Ogden, UT, June 3-7.

Minnis, P., D. F. Young, B. A. Wielicki, D. P. Kratz, P. W. Heck, S. Sun-Mack, Q. Z. Trepte, Y. Chen, S. L. Gibson, R. R. Brown, 2002: Seasonal and diurnal variations of cloud properties derived for CERES from VIRS and MODIS data. *Proc. 11th AMS Conf. Atmos. Rad.*, Ogden, UT, June 3-7, 20-23.

Sun-Mack, S., Y. Chen, T. D. Murray, P. Minnis, and D. F. Young, 1999: Visible clear-sky and near-infrared surface albedos derived from VIRS for CERES. *Proc. AMS 10th Conf. Atmos. Rad.*, Madison, WI, June 28 – July 2, 422-425.

Suttles, J. T., R. N. Green, P. Minnis, G. L. Smith, W. F. Staylor, B. A. Wielicki, I. Walker, D. F. Young, V. R. Taylor, and L. L. Stowe, 1988: Angular radiation models for Earth-atmosphere system, Vol. 1, Shortwave radiation. *NASA RP-1184*, 144 pp.

Trepte, Q., Y. Chen, S. Sun-Mack, P. Minnis, D. F. Young, B. A. Baum, P. W. Heck, 1999: Scene identification for the CERES cloud analysis subsystem. *Proc. AMS10th Conf. Atmos. Rad.*, 28 June – 2 July, Madison, WI.

Wielicki, B. A., Barkstrom, B. R., Baum, B. A., Charlock, T. P., Green, R. N., Kratz, D. P., Lee, R. B., Minnis, P., Smith, G. L., Young, D. F.; Cess, R. D.; Coakley, J. A.; Crommelynck, D. A. H.; Donner, L.; Kandel, R.; King, M. D.; Miller, A. J.; Ramanathan, V.; Randall, D. A.; Stowe, L. L.; and Welch, R. M., Clouds and the Earth's Radiant Energy System (CERES): Algorithm Overview. *IEEE Transactions on Geoscience and Remote Sensing*, **36**, July 1998, pp. 1127-1141.